Dynamic Changes in the Structure, Chemical State and Catalytic Selectivity of Cu Nanocubes during CO_2 electroreduction: Size and Support Effects

Philipp Grosse[1⊥], Dunfeng Gao[1⊥], Fabian Scholten[1], Ilya Sinev[1], Hemma Mistry[1,2], Beatriz Roldan Cuenya[1,2,3*]

[1] Department of Physics, Ruhr-University Bochum, 44780 Bochum, Germany.

[2] Department of Physics, University of Central Florida, Orlando, Florida 32816, USA.

[3] Department of Interface Science, Fritz-Haber Institute of the Max Planck Society, 14195 Berlin, Germany

*e-mail: Roldan@fhi-berlin.mpg.de

[⊥] equally contributing 1st authors.

Abstract

In situ and *operando* spectroscopic and microscopic methods were used to gain insight into the correlation between the structure, chemical state, and reactivity of size- and shape-controlled ligand-free Cu nanocubes (Cu-cubes) during CO_2 electroreduction (CO_2RR). Dynamic changes in the morphology and composition of Cu-cubes supported on carbon were monitored under potential control via electrochemical atomic force microscopy, X-ray absorption fine-structure spectroscopy and X-ray photoelectron spectroscopy. Under reaction conditions, the roughening of the nanocube surface, disappearance of the (100) facets, formation of pores, loss of Cu and reduction of CuO_x species observed were found to lead to a suppression of the selectivity for multi-carbon products (i.e. C_2H_4 and ethanol) versus CH_4. A comparison with Cu-cubes supported on Cu foils revealed an enhanced morphological stability and persistence of Cu(I) species under CO_2RR. Both factors are held responsible for the higher C_2/C_1 product ratio observed for the Cu cubes/Cu as compared to Cu cubes/C. Our findings highlight the importance of the structure of the active nanocatalyst but also its interaction with the underlying substrate in CO_2RR selectivity.

Introduction

Since a number of years there is an increasing interest in trying to understand the parameters that govern the electrochemical reduction of CO_2 (CO_2RR) to design catalysts with high selectivity for valuable chemicals and fuels.[1] Among these parameters, the catalyst structure and chemical state are of particular importance.[2–4] Compared to polycrystalline Cu electrodes, nanostructured Cu catalysts have shown a significantly improved CO_2RR performance, attributed to grain boundaries[5,6], Cu(100) facets[7–12], increased roughness[13], defects[14–16], low-coordinated sites[17–19], and the presence of subsurface oxygen and Cu(I) species[20–29].

Previous studies[9–11] on Cu single crystals have shown the improved C-C coupling performance of (100) facets, which was further confirmed by the high selectivity towards ethylene observed on cubic-shaped Cu catalysts[7,8,16,21,30–36]. However, the presence of (100) facets is not the only factor responsible for the superior activity and selectivity of cubic-shaped Cu catalysts, with surface roughness, subsurface oxygen and Cu(I) species or Cu/Cu(I) interfaces formed and/or stabilized under reaction conditions also playing a very important role.[21] The function of oxygen in such structures is particularly intriguing, since on Cu(100) surfaces it was discussed to contribute to the formation of oxygenated hydrocarbons[37]. The complexity arising from the multiple factors affecting the catalytic performance of cubic-shaped Cu catalysts requires a systematic study of the evolution of their structure and oxidation state under *operando* CO_2RR conditions.

This work focuses on the understanding of the relative importance of the different factors responsible for specific selectivity trends observed for Cu catalysts during CO_2RR, namely, the presence and stability of Cu(100) facets, defect sites, and the content of Cu(I) species and/or subsurface oxygen. By electrochemically growing ligand-free Cu-cubes on C supports and comparing with analogous samples supported on Cu foils, we were able to reveal the intrinsic behavior of the cubic-shaped Cu NPs catalysts and their dynamic evolution under CO_2RR conditions.

Results and Discussion

Size-dependent changes in the morphology and composition of Cu-cube samples electrodeposited on carbon paper were investigated *ex situ* via scanning electron microscopy (SEM) and energy dispersive X-ray spectroscopy (EDX) before and after CO_2RR, Figures 1, S1 and S2 (Suppl. docs). In all samples the Cu-cubes were found to decrease in size in the course of the first 1 h of the reaction. Furthermore, in this process the originally flat facets and sharp edges of the Cu-cubes were found to roughen, resulting in a porous nanocube surface, Fig. 1.

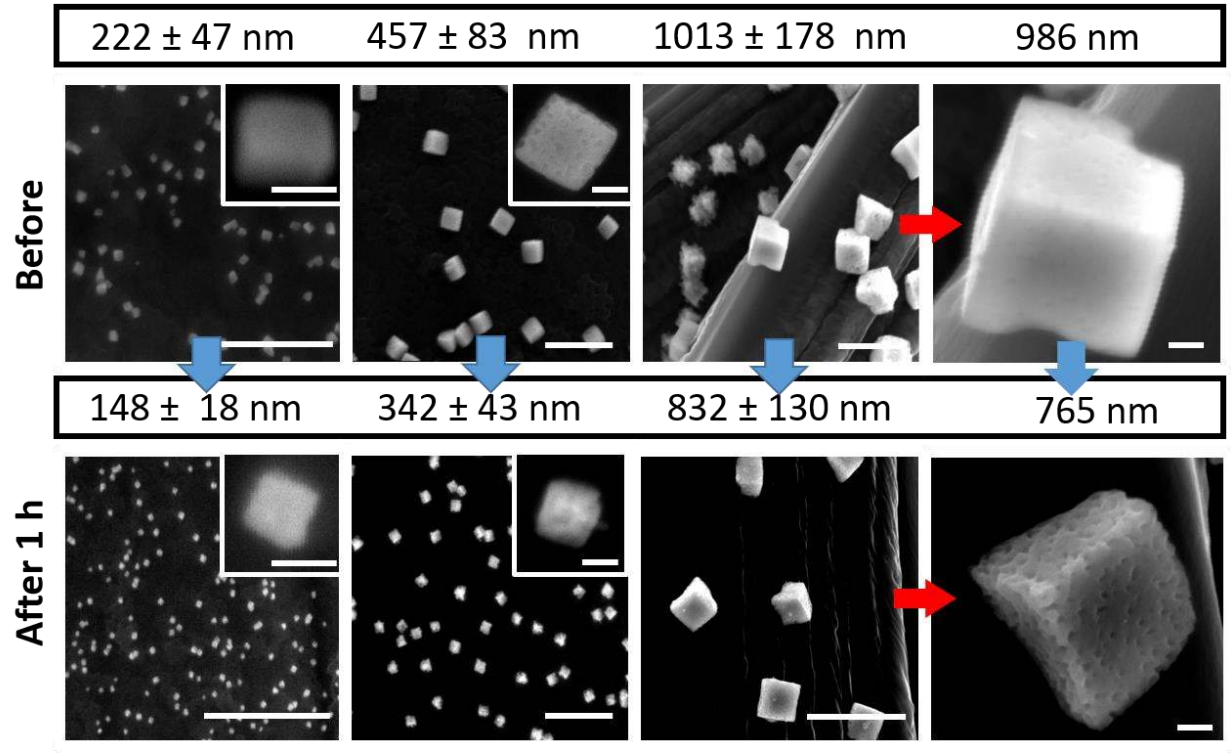

Figure 1: SEM images from size-controlled Cu-cube samples electrodeposited on carbon paper acquired before and after CO_2RR at -1.05 V for 1 h. The scale bars in the main panels are 2 µm, those in the insets and in the images of the last column are 200 nm.

Operando electrochemical atomic force microscopy (EC-AFM) measurements carried out on a sample with ~100 nm large cubes also revealed significant changes in their morphology already prior to the actual CO_2RR. Sample immersion in the aqueous 0.1 M $KHCO_3$ electrolyte at open circuit potential was observed to lead to the formation of "cracks" on the cube facets. These cracks are likely the result of mechanical stress taking place during the solvation of Cl^- ions while being transferred from the cubes to the electrolyte. SEM-EDX data revealed that Cl

was present throughout the entire Cu volume in the as prepared samples and therefore, the loss of Cl leads to drastic structural changes in the entire cube volume.

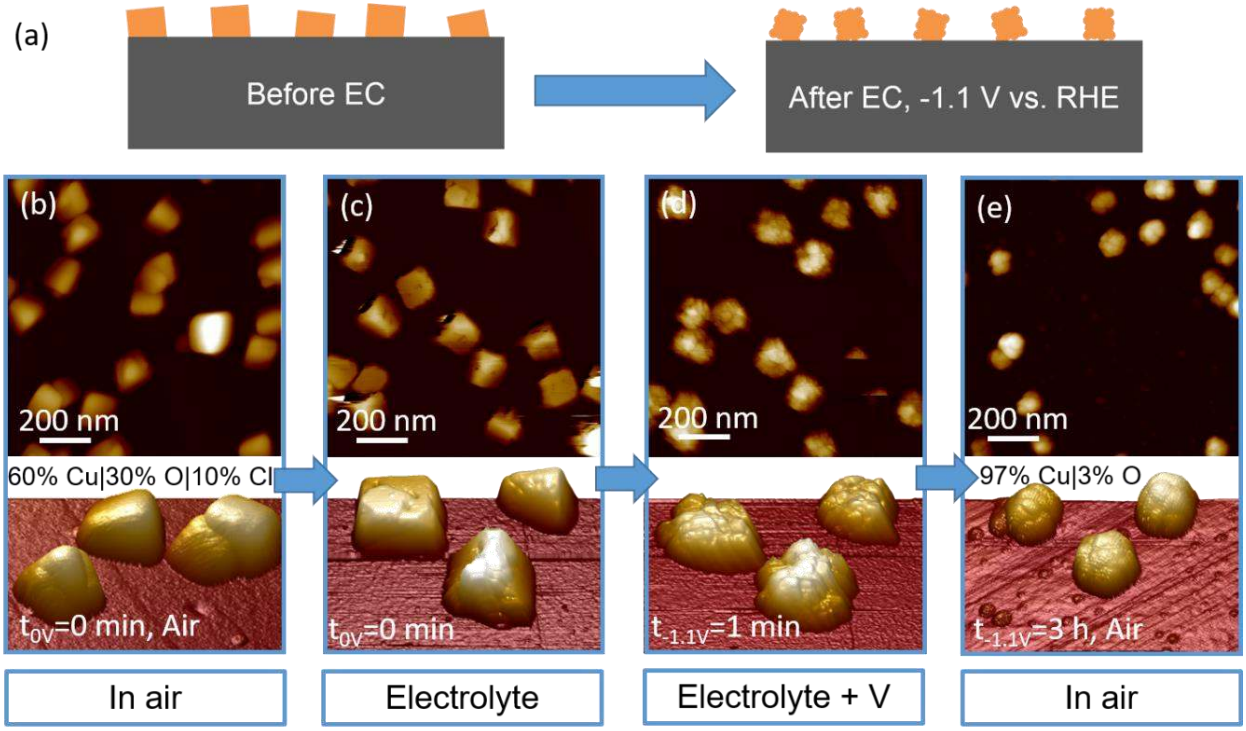

Figure 2: (a) Schematic representation of the morphological evolution of Cu-cube catalysts. (b-e) AFM images of Cu-cubes electrodeposited on highly oriented pyrolytic graphite (HOPG) acquired in air (b), and *operando* EC-AFM measurements in a CO_2-saturated 0.1 M $KHCO_3$ aqueous solution at open circuit potential (c), at -1.1 V vs RHE in the same electrolyte for 1 min (d), and after 3 h under the same conditions as in (d) and subsequent air exposure (e).

A 1 min potential pulse at -1.1 V vs RHE resulted in the further roughening of the nanocube surface, loss of sharp corners and edges, and a decrease in the edge length of approximately 10 %. The latter is assigned to the initial reduction of Cu_2O to Cu as well as some loss of Cu. After 3h CO_2RR at -1.1 V vs RHE, an additional 10% decrease of the NP size was observed, with rough spherical-like NP shapes.

X-ray induced Cu LMM Auger electron spectra (XAES) were acquired from pristine C-supported Cu-cubes (220 nm) before and after CO_2RR for 1 h at -1.1 V vs RHE in an ultrahigh vacuum (UHV) XPS system directly interfaced to an electrochemical cell. Thus, the sample could be transferred in vacuum to avoid re-oxidation.[21] Additional Cu-2p XPS data are also

included in Figure S3. A surface composition of the pristine C-supported Cu-cubes of 52% Cu_2O, 22% $CuCl_2$, 23% CuCl, and 3% metallic Cu was obtained before reaction, Fig. 3. After the electrochemical treatment, the cubes are mostly reduced, with only 4.6% Cu_2O detected. Interestingly, a higher content of Cu(I) species (13%) was detected after CO_2RR on similarly synthesized Cu-cubes supported on a Cu-foil, and no Cu(I) at all in the pristine Cu foil support after CO_2RR (Fig. S4). The latter finding highlights the key role of having a Cu cube/Cu foil interaction for the stabilization of Cu(I) species.

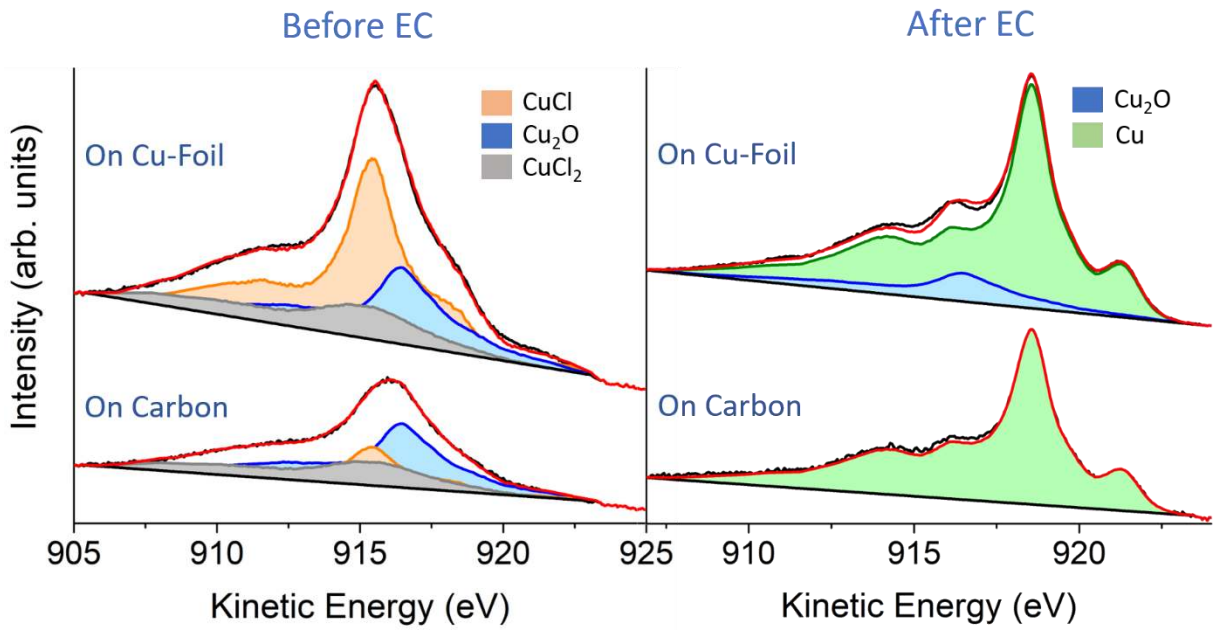

Figure 3: *Quasi in situ* Cu Auger LMM XAES spectra of 220 nm Cu-cubes electrodeposited on C paper and 250 nm cubes deposited on a Cu-foil acquired before (left) and after 1 hour of CO_2RR at -1.1 V vs RHE (right).

To gain further insight into the stability of Cl, Cu(I) species, and subsurface oxygen in our Cu-cubes under CO_2RR, *operando* X-ray absorption fine-structure (XAFS) measurements were conducted on 120 nm Cu-cubes, Figures 4 and 5 (see also Figs. S5, S6, and S7 in the SI for more details). As compared to XPS and XAES, probing about 10 nm below the surface, XAFS is a bulk sensitive technique that reveals the overall change in the structure and composition of the Cu-cubes. The as prepared state of the Cu-cubes shows a mixture of Cu_2O and $CuCl_x$, which almost immediately changes fully into Cu_2O upon becoming in contact with the electrolyte.

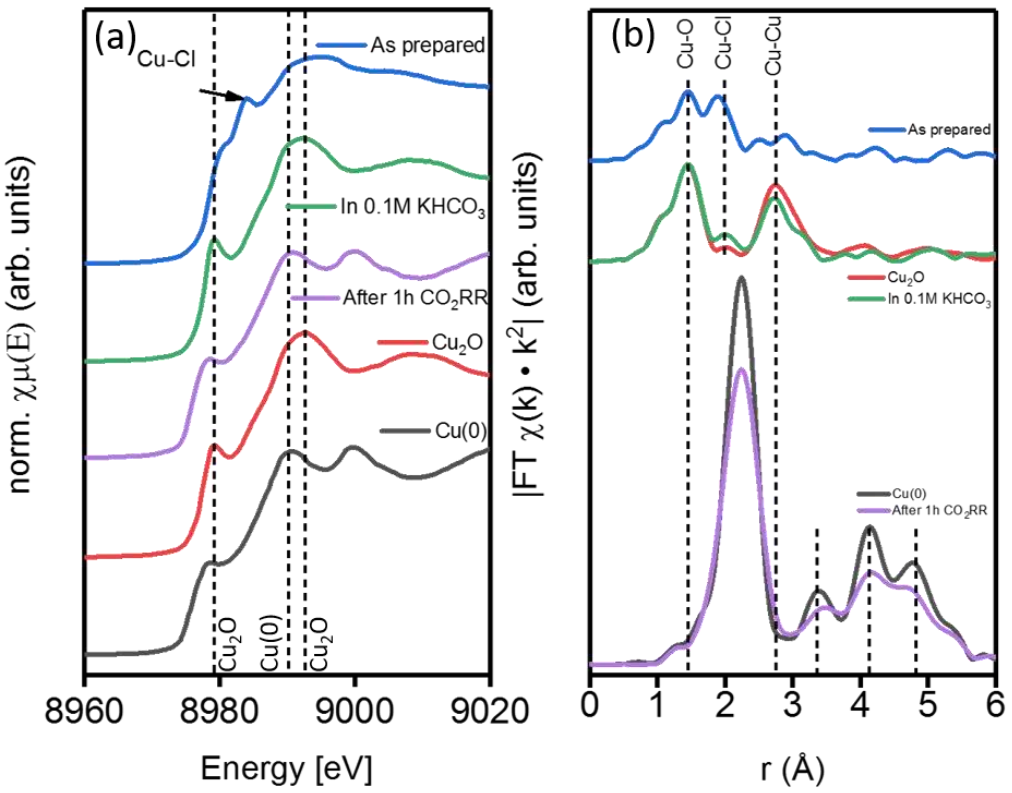

Figure 4: Normalized XANES region (a) and Fourier-transform magnitudes of k^2-weighted EXAFS data of pristine Cu-cubes (b) measured as prepared, in 0.1 M $KHCO_3$ at open circuit potential and in the same electrolyte after 1 h of CO_2RR at -1.1V vs RHE.

In CO_2-saturated 0.1 M $KHCO_3$, the spectrum resembles greatly the Cu_2O reference, with only a very small difference where the Cl-feature was previously observed and a small decrease of the Cu-O feature. After 1 h at -1.1 V vs RHE, the spectrum obtained for the Cu-cubes resembles that of metallic Cu. The Fourier Transform (FT) data obtained for the Cu-cubes in the electrolyte after 1 h CO_2RR at -1.1 V vs RHE are less intense in comparison to a bulk Cu-foil, indicating a lower atomic coordination and/or enhanced disorder. From the first shell Cu-Cu fit after 1 h of applied potential, a coordination number (CN) of 10.8 was obtained for the Cu-cubes (vs 12 expected for bulk fcc-Cu). The lower CN values might be indicative of the formation and growth of pores on the Cu-cubes under reaction conditions or the partial disruption of the nanocubes, leading to an increased surface roughness. The *operando* EC-AFM data also revealed the formation of cracks (defects) on the Cu-cubes even before applying the potential once they were exposed to the electrolyte. The porous structure seen by SEM can also be a result of the

progressive CuO_x reduction during the reaction. Under reaction conditions, these pores as well as the cube corner and edges appear more prone to dissolution than the higher coordinated flat facets.

Since Cu(I) species[37] have been suggested to play an important role in CO_2RR selectivity, in order to better detect small amounts of Cu-O species an additional analysis of the XAFS data by wavelet-transform[38] (WT) was applied (Fig. 5). Details on this analysis are given in the Suppl. documents. After processing the measured spectra and doing the Morlet WT, the spectra were normalized to the highest signal, allowing subtraction of measured reference materials. The Cu-cubes on C in their as prepared state display a large feature at R ~ 1.4 Å and k ~ 3.9 $Å^{-1}$ which represents the Cu-O shell, whereas at a slightly higher distance (R ~ 2 Å, k ~ 7 $Å^{-1}$) the interaction of Cu with the heavier Cl atoms is visible. For the as prepared sample, only a faint Cu-Cu 1st and 2nd neighbor interaction is observed after the subtraction of a Cu_2O reference from the pristine Cu-cubes, indicating that the sample consists almost exclusively of Cu_2O and $CuCl_x$. In the electrolyte, the $CuCl_x$ feature immediately disappears and a Cu-O-Cu feature arises at R ~ 3 Å and k ~ 4 $Å^{-1}$. In addition, the magnitude of the Cu-O component decreases slightly. After 1 hour of CO_2RR, the most prominent feature is that of the Cu-Cu first shell (R ~ 2.3 Å, k ~ 7 $Å^{-1}$). The pristine Cu-cubes resemble almost exactly the metallic Cu reference after 1 h of CO_2RR. A deconvolution of the Cu XANES region of pristine Cu-cubes in 0.1 M $KHCO_3$ with Cu, Cu_2O, and CuO standards, Fig. S7, yields a composition of 99% Cu and 1% (within the error margin) Cu_2O after 1 h of CO_2RR. CuO could not be reasonable fitted. These findings are in good accordance with the XPS surface analysis indicating that for the Cu cube/C system, no Cu_2O species remain after 1 h of reaction either at the surface (XPS) or in sub-surface regions (XAFS), which is in clear contrast with previous findings for Cu-cubes/Cu-foil (Fig. 3). [21,22]

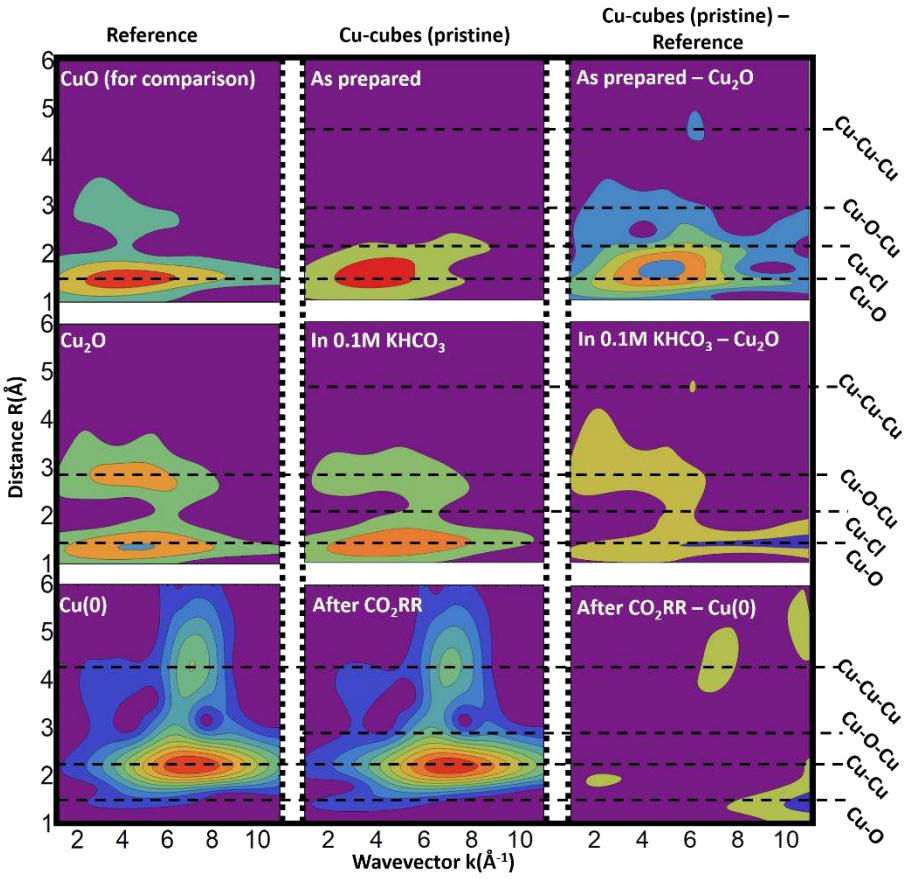

Figure 5: Wavelet transform of Cu-cubes as prepared, in 0.1 M $KHCO_3$, and after 1 h of CO_2RR as well as the bulk references used. The height is normalized to 1 and the subtracted images scaled by a factor of two for better visibility.

After observing drastic changes in the morphology and chemical composition of the samples under *operando* reaction conditions within the first 1-3 hours, the electrochemical performance was studied in order to gain insight into structure/chemical-state/reactivity correlations. The background signal from the C-paper support was subtracted from all data presented as shown in Fig. S8. A comparison between HER Faradaic efficiency (parasitic reaction) and the sum of the Faradaic efficiency of all products from CO_2RR is displayed in Fig. 6. Detailed information on the different products detected can be found in Figure 7 for the 220 nm Cu-cubes and in Figs. S9, S10 and S11. Similar trends for small Cu-Au cubic NPs were reported in Ref.[39].

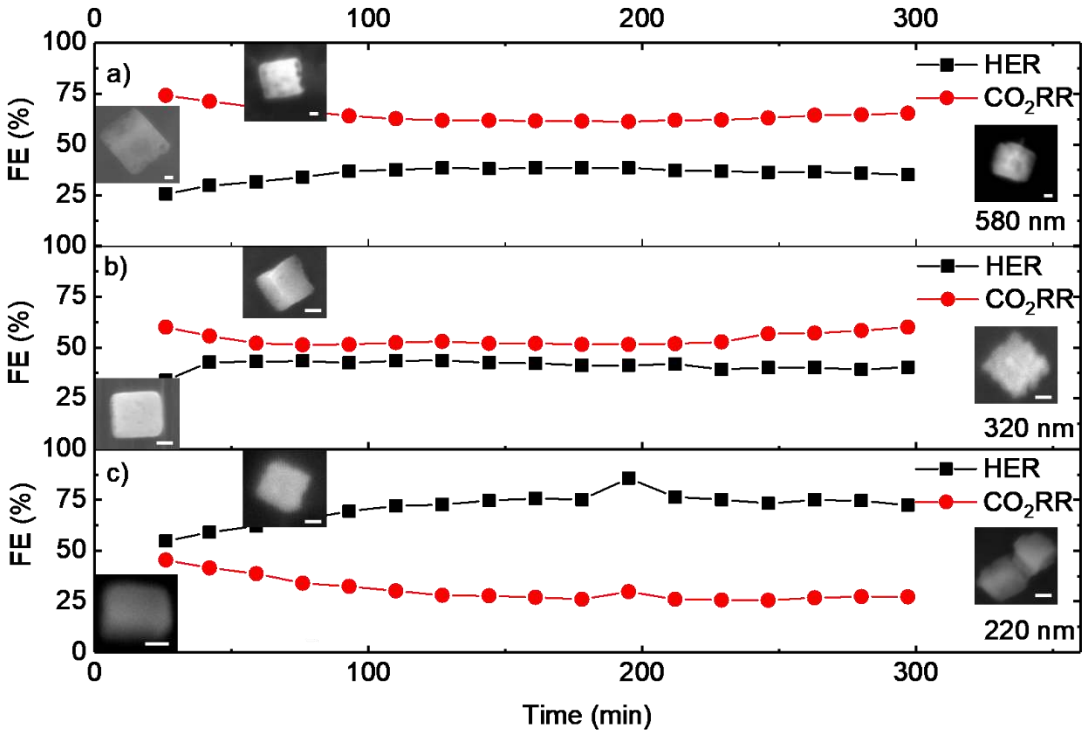

Figure 6: Faradaic efficiency for CO_2RR and HER at approx. -1.05 V vs RHE recorded during 5 h for samples with different Cu-cube sizes (580 nm, 320 nm and 220 nm). The insets display SEM images of typical Cu-cubes measured after different reaction times. The size of the scale bars is: 100 nm.

For the stability tests, Cu-cubes of three different initial sizes were investigated at -1.05 V vs RHE, Fig. 6. This potential was chosen since we expect to see the highest selectivity towards C_2-C_3 products.[40] The total CO_2RR FE was found to increase with increasing Cu-cube size, and achieves an initial value of ~75% on the 580 nm cubes. This is assigned to the enhanced morphological stability of the larger cubes. A second general trend, independent of size, is a decrease in Faradaic efficiency for CO_2RR and increase in HER over time. An exception is the 220 nm Cu-cubes sample, which starts already with higher Faradaic efficiency for HER over CO_2RR. The smaller cube size on the weakly binding C support leads to a lower stability of the Cu-cubes, leading to the loss of material into the electrolyte and possible subsequent re-deposition as small clusters on the support and Cu-cubes. Such low-coordinated structures were found to result in an increase in the H_2 and CO production and decrease in the formation of hydrocarbons, i.e., they favor HER over CO_2RR.[41,42] This correlates with the observed

morphological changes shown in Figs. 1 and 2, where a rounding of corners and edges and roughening of the facets is observed.

Figure 7(a) displays the FE data for the pristine 220 nm Cu-cubes on C measured as a function of the applied potential after 1 h of CO_2RR. The production of C_2 and C_3 products peaks around -1.0 V vs RHE, whilst hydrogen evolution is the lowest at this potential. At potentials more negative than -1.0 V vs RHE, C_2/C_3 products decline, whilst methane production keeps increasing.

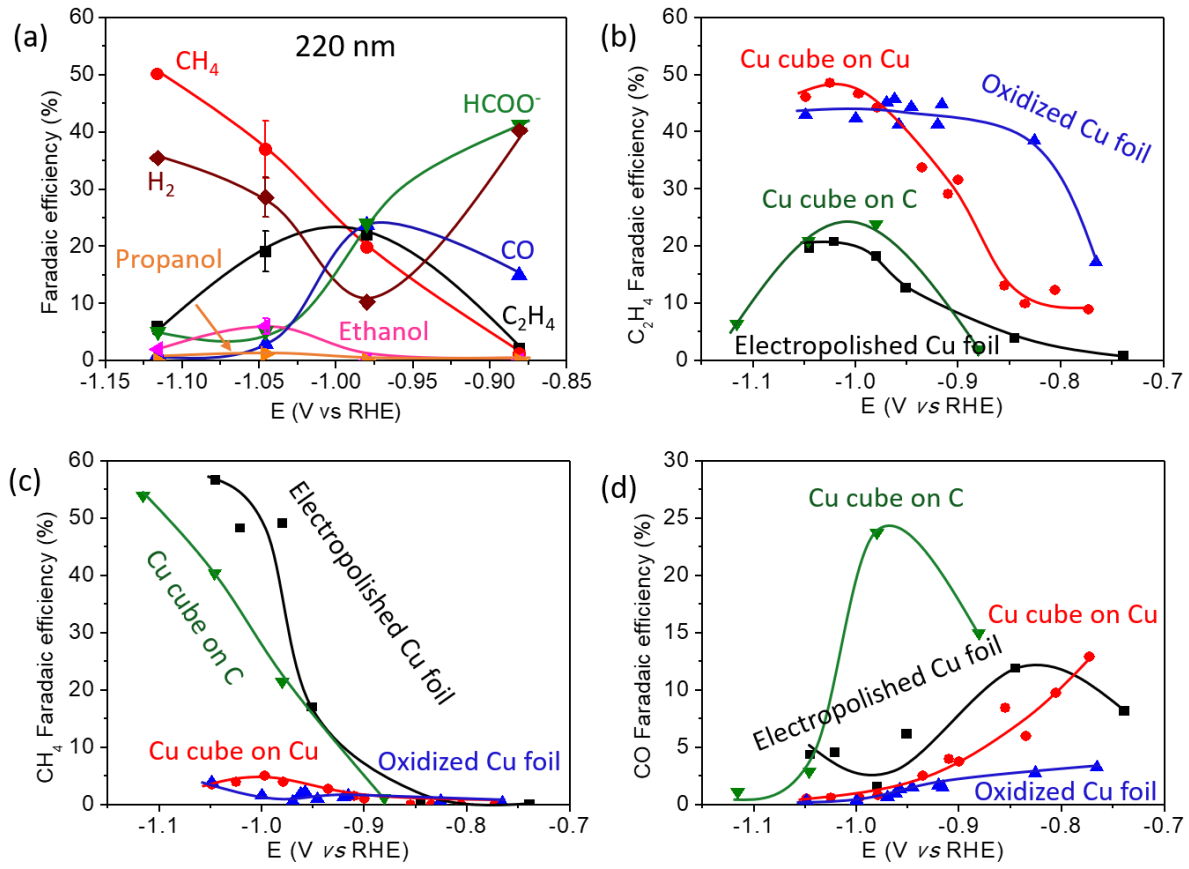

Figure 7: (a) Faradaic efficiency of pristine 220 nm Cu-cubes on C as a function of applied potential obtained after 1 h of CO_2RR. Faradaic efficiencies for C_2H_4 (b), CH_4 (c), and CO (d) are also shown for the pristine 220 nm Cu-cubes on C, 250 nm Cu-cubes on Cu foil and two reference Cu foils electropolished and O_2-plasma treated (20, 20 W, 400 mTorr[21,22]).

The FE for C_2H_4, CH_4 and CO as a function of the applied potential for the pristine 220 nm Cu-cubes on C together with similarly synthesized 250 nm Cu-cubes supported on a Cu foil as

well as electropolished and O_2-plasma-treated Cu foils are shown in Figure 7(b-d). A very strong support-effect is evident, with the Cu-cubes grown in the weakly-interacting C support displaying a higher overpotential and much lower FE for C_2-C_3 products than the similarly-sized Cu-cubes on the Cu foil. In fact, as can be seen in Fig.7(c), the production of CH_4 of the Cu-cubes on C resembles the metallic electropolished Cu foil, although the CO production of the Cu-cubes on C is much higher, Fig. 7(d). It is remarkable that the pristine Cu-cubes on the Cu-foil, which were found to better stabilize Cu(I) species under reaction conditions (Fig. 3), behave similarly to the O_2-plasma treated Cu foils. Therefore, we can confirm a direct correlation between the stabilization of Cu(I)/Cu interfaces (Cu-cubes on Cu-foil) and the selectivity for C_2-C_3 products, since metallic Cu-cubes supported on C are more selective for C_1 products. This is however not the only reason for the change in the selectivity. Even more important are the drastic structural changes observed for the Cu-cubes on C. The roughening of the Cu(100) facets, partial loss of the cubic shape and formation of pores as well as detachment from the surface play a critical role in the selectivity switch reported here.

2. Conclusion

A simple electrochemical method for the synthesis of cubic-shaped nanoparticles of tunable size supported on carbon substrates is presented here. Dynamic morphological and chemical transformations of Cu-cubes during CO_2RR were monitored using *operando* EC-AFM and X-ray absorption fine-structure spectroscopy (XAFS). Drastic changes in the cube morphology were found to take place for the Cu-cubes on C under CO_2RR conditions, including the roughening and loss of (100) facets, loss of Cu atoms from edge and corner sites, and the reduction of CuO_x species.

The selectivity for CO_2RR versus HER was found to decrease with decreasing cube size, which was assigned to more drastic changes in the cube morphology taking place under CO_2RR conditions over smaller cubes. In contrast with the findings previously reported for Cu-cubes grown on Cu foils, a surprisingly high selectivity for CH_4 as compared to C_2H_4 was observed when deposited on C. The observed morphological instability of the Cu-cubes on C versus those deposited on Cu, together with the absence of stable Cu(I) species in the former samples are considered responsible for the preferred selectivity for C_1 products.

Experimental

A mixture of 5 mM copper sulfate-pentahydrate ($CuSO_4 \cdot 5H2O$) and 5 mM potassium chloride (KCl) was used as starting material. Electrochemical cycling between an oxidizing (+0.55 V vs. RHE) and a reducing potential (+0.22 V vs. RHE) with varying number of cycles (1-100), depending on the desired cube size and coverage, lead to the electrodeposition of size- and shape-controlled Cu-cubes with a narrow size distribution. Initially, a potential of -0.2 V vs Ag/AgCl was held for 8 s with a subsequent ramp to +0.4 V vs Ag/AgCl for 4 s at a ramp rate of 700 mV/s. Returning to the initial potential completes the cyclic voltammetry. Cu-cube sizes ranging from 80 nm to 1,2 µm were obtained depending on the 1 mM-100 mM KCl and $CuSO_4 \cdot 5H_2O$ concentration, number of cycles, and applied potential. High surface area carbon paper was used as substrate (Toray Carbon Paper TGP-H-060). The Cu-cubes on Cu-foil were prepared as described in Ref. [21].

Acknowledgment

This work was funded by the Cluster of Excellence RESOLV at RUB (EXC 1069) supported by the Deutsche Forschungsgemeinschaft and the German Federal Ministry of Education and Research (Bundesministerium für Bildung und Forschung BMBF) under grant #03SF0523C-'CO2EKAT' and by the European Research Council (ERC-725915, OPERANDOCAT). Partial financial support from the U.S. National Science Foundation (NSF-Chemistry 1213182) is also greatly appreciated. The XAFS experiments were performed on beamline BM25A at the European Synchrotron Radiation Facility (ESRF), Grenoble, France. We are grateful to Aida Serrano Rubio and Germán Castro at the ESRF for providing assistance in using beamline BM25A.

3. References

[1] Y. Hori, A. Murata, R. Takahashi, S. Suzuki, *J. Chem. Soc. Chem. Commun.* **1988**, *109*, 17.

[2] H. Mistry, A. S. Varela, S. Kühl, P. Strasser, B. R. Cuenya, *Nat. Rev. Mater.* **2016**, *1*, 16009.

[3] R. Kortlever, J. Shen, K. J. P. Schouten, F. Calle-Vallejo, M. T. M. Koper, *J. Phys. Chem. Lett.* **2015**, *6*, 4073–4082.

[4] G. O. Larrazábal, A. J. Martín, J. Pérez-Ramírez, *J. Phys. Chem. Lett.* **2017**, *8*, 3933–3944.

[5] C. W. Li, M. W. Kanan, *J. Am. Chem. Soc.* **2012**, *134*, 7231–7234.

[6] A. M. Appel, *Nature* **2014**, *508*, 460–461.

[7] F. S. Roberts, K. P. Kuhl, A. Nilsson, *Angew. Chem. Int. Ed.* **2015**, *54*, 5179–5182.

[8] A. Loiudice, P. Lobaccaro, E. A. Kamali, T. Thao, B. H. Huang, J. W. Ager, R. Buonsanti, *Angew. Chem. Int. Ed.* **2016**, *55*, 5789–5792.

[9] K. J. P. Schouten, E. Pérez Gallent, M. T. M. Koper, *ACS Catal.* **2013**, *3*, 1292–1295.

[10] F. Calle-Vallejo, M. T. M. Koper, *Angew. Chem.* **2013**, *125*, 7423–7426.

[11] J. H. Montoya, C. Shi, K. Chan, J. K. Nørskov, *J. Phys. Chem. Lett.* **2015**, *6*, 2032–2037.

[12] D. Kim, C. S. Kley, Y. Li, P. Yang, *Proc. Natl. Acad. Sci.* **2017**, *114*, 10560–10565.

[13] R. Kas, R. Kortlever, H. Yilmaz, M. T. M. Koper, G. Mul, *ChemElectroChem* **2015**, *2*, 354–358.

[14] W. Tang, A. A. Peterson, A. S. Varela, Z. P. Jovanov, L. Bech, W. J. Durand, S. Dahl, J. K. Nørskov, I. Chorkendorff, *Phys. Chem. Chem. Phys.* **2012**, *14*, 76–81.

[15] R. B. Sandberg, J. H. Montoya, K. Chan, J. K. Nørskov, *Surf. Sci.* **2016**, *654*, 56–62.

[16] I. Zegkinoglou, A. Zendegani, I. Sinev, S. Kunze, H. Mistry, H. S. Jeon, J. Zhao, M. Y.

Hu, E. E. Alp, S. Piontek, et al., *J. Am. Chem. Soc.* **2017**, *139*, 14360–14363.

[17] R. Reske, H. Mistry, F. Behafarid, B. Roldan Cuenya, P. Strasser, *J. Am. Chem. Soc.* **2014**, *136*, 6978–6986.

[18] H. Mistry, F. Behafarid, R. Reske, A. S. Varela, P. Strasser, B. Roldan Cuenya, *ACS Catal.* **2016**, *6*, 1075–1080.

[19] H. Mistry, R. Reske, P. Strasser, B. Roldan Cuenya, *Catal. Today* **2017**, *288*, 30–36.

[20] H. Mistry, A. S. Varela, C. S. Bonifacio, I. Zegkinoglou, I. Sinev, Y. W. Choi, K. Kisslinger, E. A. Stach, J. C. Yang, P. Strasser, et al., *Nat. Commun.* **2016**, *7*, 12123.

[21] D. Gao, I. Zegkinoglou, N. J. Divins, F. Scholten, I. Sinev, P. Grosse, B. Roldan Cuenya, *ACS Nano* **2017**, *11*, 4825–4831.

[22] D. Gao, F. Scholten, B. Roldan Cuenya, *ACS Catal.* **2017**, *7*, 5112–5120.

[23] C. Reller, R. Krause, E. Volkova, B. Schmid, S. Neubauer, A. Rucki, M. Schuster, G. Schmid, *Adv. Energy Mater.* **2017**, *7*, 1602114.

[24] A. Eilert, F. Cavalca, F. S. Roberts, J. Osterwalder, C. Liu, M. Favaro, E. J. Crumlin, H. Ogasawara, D. Friebel, L. G. M. Pettersson, et al., *J. Phys. Chem. Lett.* **2017**, *8*, 285–290.

[25] S. Lee, D. Kim, J. Lee, *Angew. Chem. Int. Ed.* **2015**, *54*, 14701–14705.

[26] D. Ren, Y. Deng, A. D. Handoko, C. S. Chen, S. Malkhandi, B. S. Yeo, *ACS Catal.* **2015**, *5*, 2814–2821.

[27] H. Xiao, W. A. Goddard, T. Cheng, Y. Liu, *Proc. Natl. Acad. Sci.* **2017**, *114*, 6685–6688.

[28] M. Favaro, H. Xiao, T. Cheng, W. A. Goddard, J. Yano, E. J. Crumlin, *Proc. Natl. Acad. Sci.* **2017**, *114*, 6706–6711.

[29] X. Wang, A. S. Varela, A. Bergmann, S. Kühl, P. Strasser, *ChemSusChem* **2017**, *10*, 4642–4649.

[30] Z. W. Ulissi, M. T. Tang, J. Xiao, X. Liu, D. A. Torelli, M. Karamad, K. Cummins, C.

Hahn, N. S. Lewis, T. F. Jaramillo, et al., *ACS Catal.* **2017**, *7*, 6600–6608.

[31] X. Liu, J. Xiao, H. Peng, X. Hong, K. Chan, J. K. Nørskov, *Nat. Commun.* **2017**, *8*, 15438.

[32] Z. W. She, J. Kibsgaard, C. F. Dickens, I. Chorkendorff, J. K. Nørskov, T. F. Jaramillo, *Science* **2017**, *355*, eaad4998.

[33] W. Ju, A. Bagger, G. P. Hao, A. S. Varela, I. Sinev, V. Bon, B. Roldan Cuenya, S. Kaskel, J. Rossmeisl, P. Strasser, *Nat. Commun.* **2017**, *8*, 944.

[34] P. De Luna, R. Quintero-Bermudez, C.-T. Dinh, M. B. Ross, O. S. Bushuyev, P. Todorović, T. Regier, S. O. Kelley, P. Yang, E. H. Sargent, *Nat. Catal.* **2018**, *1*, 103–110.

[35] K. Jiang, R. B. Sandberg, A. J. Akey, X. Liu, D. C. Bell, J. K. Nørskov, K. Chan, H. Wang, *Nat. Catal.* **2018**, *1*, 111–119.

[36] B. Eren, R. S. Weatherup, N. Liakakos, G. A. Somorjai, M. Salmeron, *J. Am. Chem. Soc.* **2016**, *138*, 8207–8211.

[37] C. S. Le Duff, M. J. Lawrence, P. Rodriguez, *Angew. Chem. Int. Ed.* **2017**, *56*, 12919–12924.

[38] J. Timoshenko, A. Kuzmin, *Comput. Phys. Commun.* **2009**, *180*, 920–925.

[39] J. Monzó, Y. Malewski, R. Kortlever, F. J. Vidal-Iglesias, J. Solla-Gullón, M. T. M. Koper, P. Rodriguez, *J. Mater. Chem. A* **2015**, *3*, 23690–23698.

[40] Y. Hori, A. Murata, R. Takahashi, *J. Chem. Soc. Faraday Trans. 1 Phys. Chem. Condens. Phases* **1989**, *85*, 2309.

[41] H. Mistry, R. Reske, Z. Zeng, Z.-J. Zhao, J. Greeley, P. Strasser, B. R. Cuenya, *J. Am. Chem. Soc.* **2014**, *136*, 16473–16476.

[42] F. Behafarid, J. Matos, S. Hong, L. Zhang, T. S. Rahman, B. Roldan Cuenya, *ACS Nano* **2014**, *8*, 6671–6681.

COMMUNICATION

A variety of *In situ* and *operando* spectroscopic and microscopic methods were used to gain insight into the correlation between the structure, chemical state, and reactivity of size- and shape-controlled ligand-free Cu nanocubes during CO_2 electroreduction. Dynamic changes in the morphology and composition of Cu nanocubes supported on carbon were monitored under potential control and correlated to product selectivity.

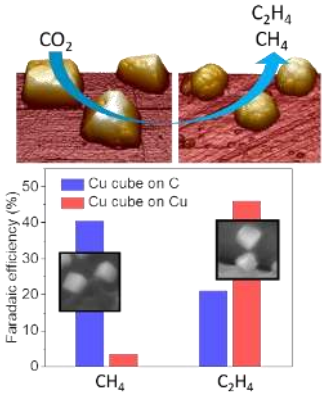

Philipp Grosse, Dunfeng Gao, Fabian Scholten, Ilya Sinev, Hemma Mistry, Beatriz Roldan Cuenya

Page No. – Page No.

Dynamic Changes in the Structure, Chemical State and Catalytic Selectivity of Cu Nanocubes during CO_2 electroreduction: Size and Support Effects

Supporting Information

1. Experimental

1.1 Sample Preparation

A mixture of 5 mM copper sulfate-pentahydrate ($CuSO_4 \cdot 5H_2O$) and 5 mM potassium chloride (KCl) was used as a starting material. Electrochemical cycling between an oxidizing and a reducing potential with varying number of cycles lead to the electrodeposition of size- and shape-controlled Cu nanocubes with a narrow size distribution. Initially, a potential of +0.55 V vs RHE was held for 8 s with a subsequent ramp to +0.22 V vs RHE for 4 s at a ramp rate of 700 mV/s. Returning to the initial potential completes the cyclic voltammetry. The number of cycles varied per sample between 1 and 100, depending on the desired cube size and respective coverage. Typically, 20 cycles are needed to get a good coverage at a small size. To tune the size further, the potentials were slightly altered. With this method, Cu-cube coverages between 15-20% were obtained on carbon paper for Cu nanocube sizes ranging from 80 nm to 1,2 µm depending on concentrations (1 mM-100 mM KCl and $CuSO_4 \cdot 5H_2O$ in a ratio of 1:1), number of cycles, and applied potential. To increase the adhesion of the Cu nanocubes to the carbon support, high surface area carbon paper was used as substrate (Toray Carbon Paper TGP-H-060).

2.1. Surface Characterization

For a thorough investigation of the surface morphology, composition, and changes during the reaction, a variety of characterization techniques were used. For morphological analysis, scanning electron microscopy (SEM) using a Quanta 200 FEG from FEI with a field emitter as electron source as well as an atomic force microscopy (AFM) using a Bruker MultiMode 8 were applied. The SEM images were acquired in vacuum utilizing a secondary electron detector (Everhart-Thornley). The images were taken with an acceleration voltage of 10 keV at a working distance of 10 mm. With these parameters, the best spatial resolution, field depth, and signal to noise ratio were achieved. For AFM, operation in air was conducted to image the initial

morphological state of the samples, with subsequent imaging in liquid under potential control using 0.1 M $KHCO_3$ as electrolyte.

The sample surface was investigated by *in-situ* X-ray photoelectron spectroscopy (XPS) in an ultra-high vacuum setup. The XPS setup was equipped with a non-monochromated Al X-ray source (hv = 1486.6 eV) as well as a hemispherical electron analyzer (Phoibos 100, SPECS GmbH). The XPS analysis chamber was connected to an *in situ* electrochemical cell (SPECS GmbH) with an Autolab potentiostat (PGSTAT 302N) to conduct the measurements, so that in between XPS measurements, the sample was not exposed to air. The Auger spectra (Fig. 3) were deconvoluted with reference signals from metallic Cu*, Cu2O (from Ref. [1]), CuCl* and CuCl2*. (* Indicates reference spectra measured in our system).

Bulk characterization was experimentally realized by energy-dispersive X-ray spectroscopy (EDX) and X-ray absorption fine-structure spectroscopy measurements (XAFS). The EDX spectra were acquired in vacuum with a liquid-N_2 cooled detector that was attached to the previously described Quanta200 FEG microscope by FEI. All data shown correspond to an average of at least three separate measurements and the error in the content of the different species was calculated from these. The samples after synthesis and reaction were washed thoroughly and transferred immediately into the SEM chamber to minimize the air exposure and thereby possible reoxidation.

Operando XAFS measurements were conducted to solidify the findings and give better accuracy about the content of the different Cu, CuO and Cu_2O species in subsurface sample regions (volume-averaging technique). For each sample, the full spectrum consisting of the X-ray absorption near-edge structure region (XANES) and the extended X-ray absorption fine structure region (EXAFS) were acquired. After subtracting a baseline for pre- and post-edge as well as a function for the edge-step, the remaining part of the spectrum in energy space (E-space) is then transferred to wavenumbers (k-space). The resulting spectrum is shown in Fig. S4. These spectra can be Fourier transformed to get the spectrum in R-space which then can be fitted. These measurements were compared to references and fitted as well. Additionally, Morlet wavelet transform (WT) was performed to better analyze small amounts of oxide species after reaction. In contrast to the traditionally applied Fourier transform (FT), the WT allows two-

dimensional separation in distance and frequency space domain simultaneously. The mathematical details regarding the application of WT are discussed by Timoshenko et. al.[2]

For electrochemical analysis, an H-type cell, with two compartments separated by a Selemion anion exchange membrane (by AGC), was used. The cell was gas-tight, both compartments were filled with 40 mL of electrolyte, and continuously purged with CO_2 at a flow rate of 20 mL min^{-1}. The electrolyte used in the experiments was a $KHCO_3$ (Sigma Aldrich, 99%) solution with a concentration of 0.1 M. This acts as a buffer to avoid significant bulk pH changes during the reaction, since this could influence the reaction pathway[3–5]. To ensure CO_2 saturation, the electrolyte was purged prior to the experiment to remove dissolved oxygen and saturate the solution. A leak-free Ag/AgCl/3.4 M KCl reference electrode by Innovative Instruments Inc., and a platinum gauze counter electrode by MaTeck (3600 mesh cm^{-2}) were used. The sample, which acts as the working electrode in this setup, was fixed with a conductive clamp. Further, all exposed parts of the clamp and the backside of the sample were covered by Kapton tape to exclude possible partaking in the reaction. Each sample was measured with a chronoamperometric step for 1 h (if not stated otherwise) at each potential. Potential control was realized with an Autolab potentiostat (PGSTAT 302N). The measured potentials were *iR*-corrected as determined by current interrupt and converted to the reversible hydrogen electrode scale. The catalytic active area was determined by estimating the surface from the SEM images (by size distribution over multiple spots).

The products from CO_2RR come in gaseous and liquid form. Gaseous products were measured every 17 min by an online gas chromatography (GC, Agilent 7890A). The products were separated by different columns (Molecular sieve 13X, HayeSep Q, and Carboxen-1010 PLOT) and subsequently quantified with a flame ionization detector (FID) as well as a thermal conductivity detector (TCD). During the reaction, liquid products as carboxylates (e.g. formate ad acetate) are formed. These liquid After 1 h of CO_2RR products were analyzed by high performance liquid chromatography (HPLC, Shimadzu Prominence), which is equipped with a NUCLEOGEL Sugar 810 column for product separation as well as a refractive index detector (RID) for quantification. In addition, alcohols were produced during the reaction, which were analyzed with liquid GC (Simadzu 2010 plus) equipped with a silica capillary column and a FID. All offline product analysis was conducted directly after the experiment. From the measured

product distribution and the current after 1 h (if not stated otherwise), the reported Faradaic efficiency (FE) were calculated.

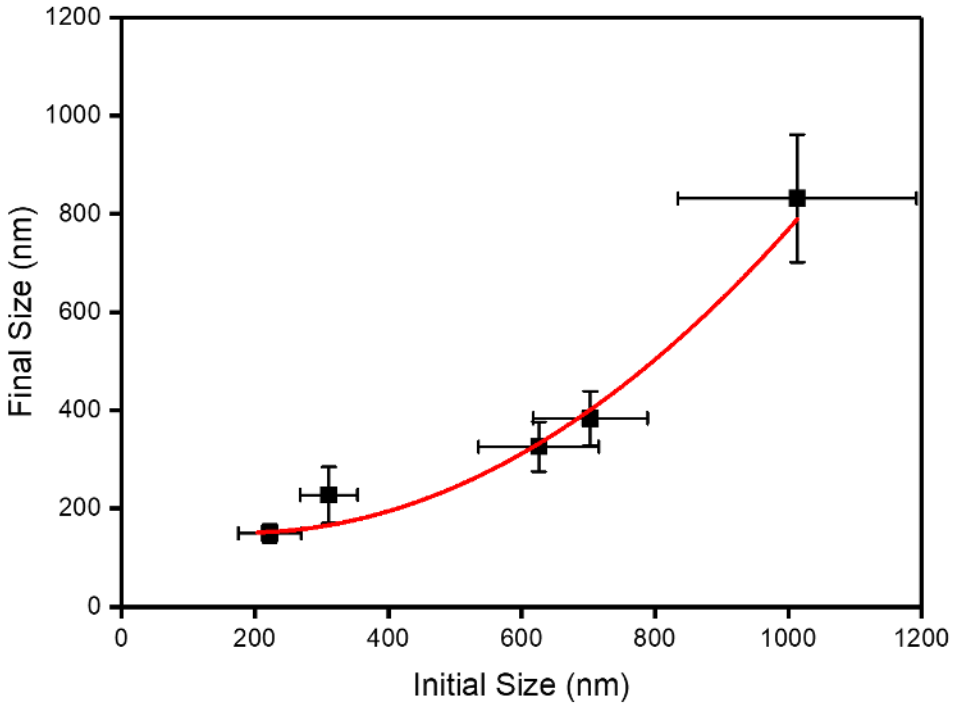

Figure S1: Cu-cube edge length measured via SEM before and after 1 hour of CO_2RR at -1.05 V vs RHE. A polynomial fit (2nd order) was applied to serve as guide for the eye. Our data indicate that the size decrease does depend on the initial cube size.

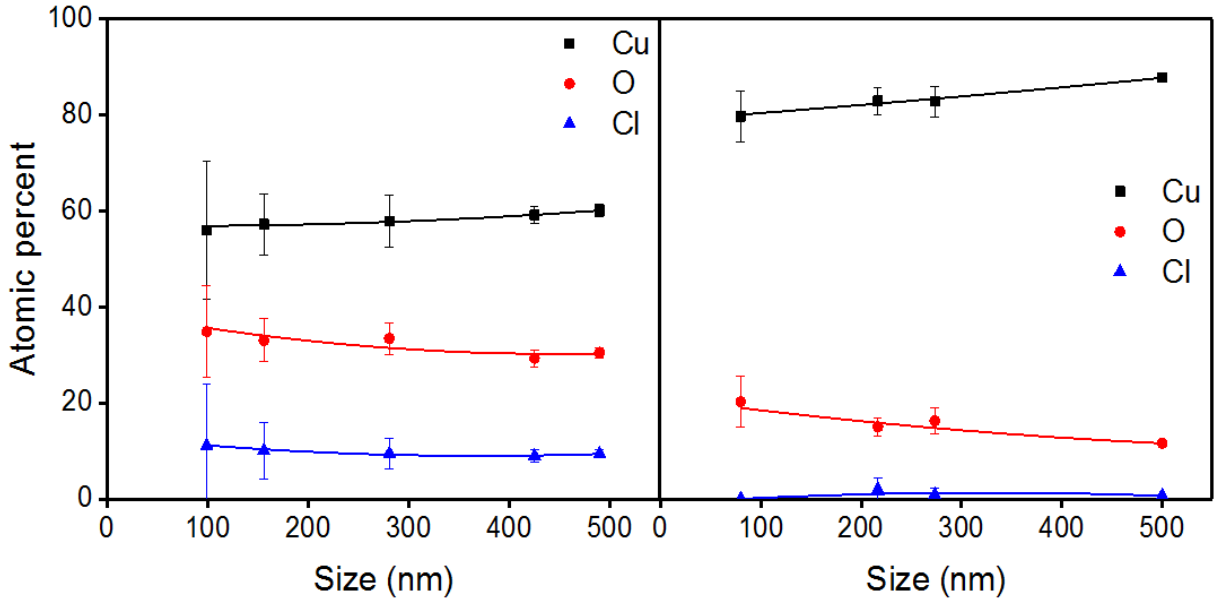

Figure S2: Comparison of single Cu-cube EDX before and after reaction and a correlation of their atomic percent. Polynomial fits of 2nd order indicate a size dependent trend, with smaller cubes containing more oxygen and initially more chlorine.

To determine the surface composition of the pristine Cu-cubes before and after CO_2RR for 1 h at -1.1 V vs RHE, X-ray photoelectron spectroscopy (XPS) data from the Cu-2p (Fig. S3) and Cu LMM Auger region (Fig. 3 in the main text) were acquired in an ultra-high vacuum-(UHV) XPS system directly attached to an electrochemical cell, allowing the transfer of the samples in vacuum to avoid reoxidation. Although no distinction between metallic Cu and Cu^+ species can be made in the analysis of the Cu-2p region (Fig. S3), our fits confirm a content of 64 % Cu(I/0), and 36 % Cu(II) in the as prepared sample and almost no Cu(II) after reaction (4 %). The Cu LMM AES data (Fig. 3) were deconvoluted using reference spectra for metallic Cu, Cu_2O, CuCl and $CuCl_2$ measured in the same system together with reference spectra by Biesinger et al.[6] Our quasi *in-situ* XPS data reveal that the surface of the pristine Cu nanocubes consisted of 51.7 % Cu_2O, 21.8 % $CuCl_2$, 23.5 % CuCl, and 3.0 % metallic Cu. After electrochemical treatment for 1 h at -1.05 V vs RHE, the XPS data (no potential applied on the sample during XPS) indicate that the cubes are mostly reduced, but ~5 % Cu_2O was still detected.

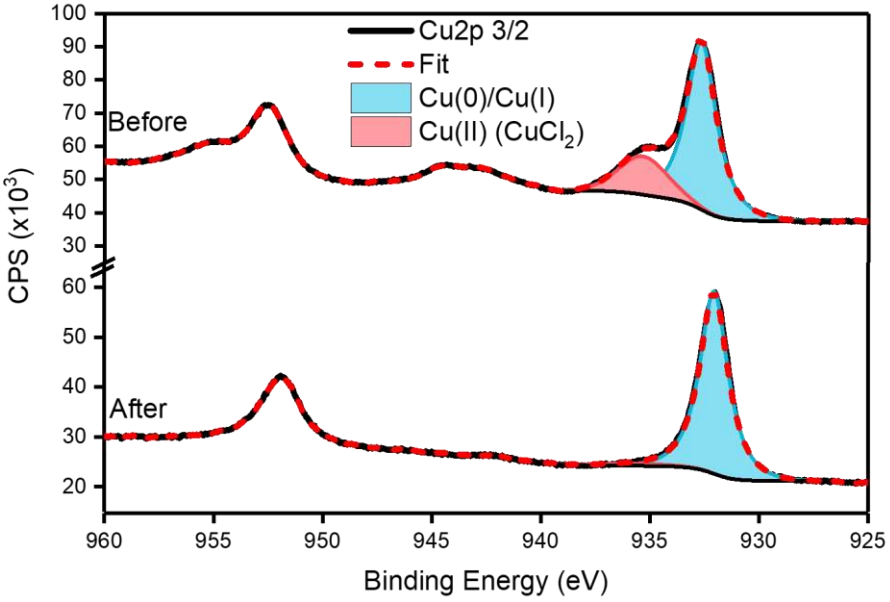

Figure S3: *Quasi in situ* XPS Cu-2p core level spectra from a pristine Cu nanocube sample and the same sample measured after 1 h CO_2RR at -1.1 V vs RHE, fitted with two doublets corresponding to Cu(0)/Cu(I) species (indistinguishable) and Cu(II). Satellite oxide features were also considered in the fits for the Cu(II) species.

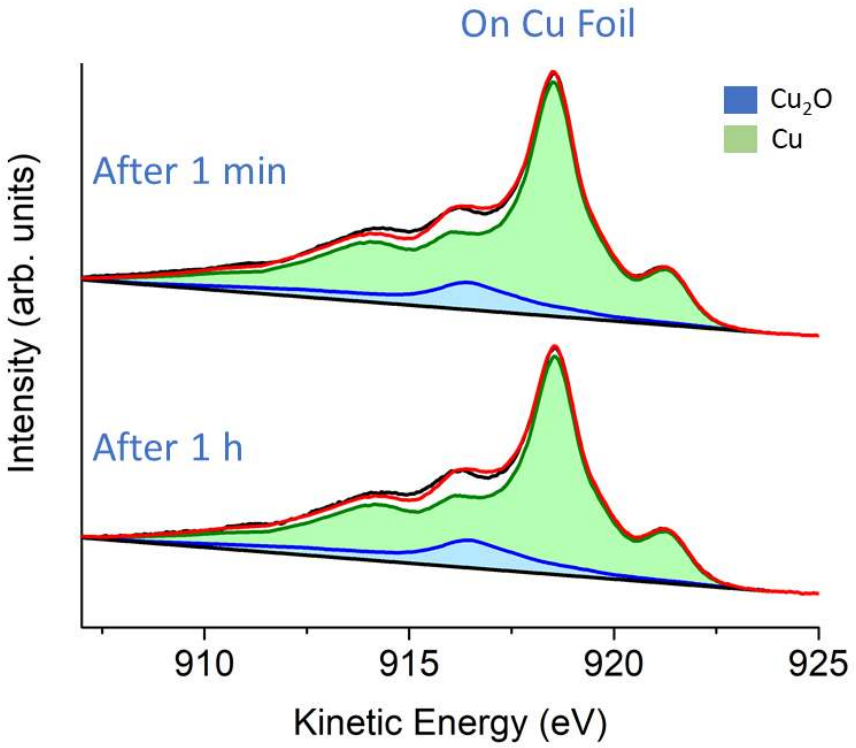

Figure S4: Cu AES LMM Spectra of 250 nm Cu-Cubes on a Cu Foil measured *quasi in situ* after 1 minute and 1 hour of CO_2RR at -1.0V vs RHE.

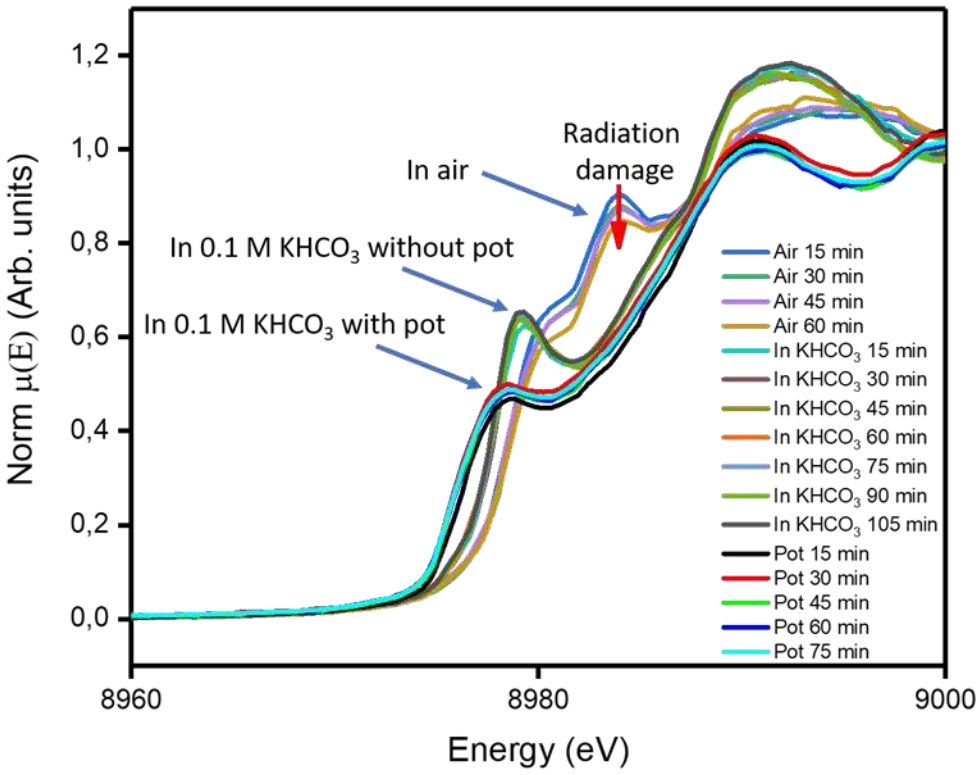

Figure S5: Operando XANES data acquired on 120 nm Cu-cubes deposited on C conducted in 15 min time steps. The individual measurements in air, in electrolyte (0.1 M $KHCO_3$) without potential and in electrolyte with potential are shown. The potential of the data shown is -1.1V vs RHE.

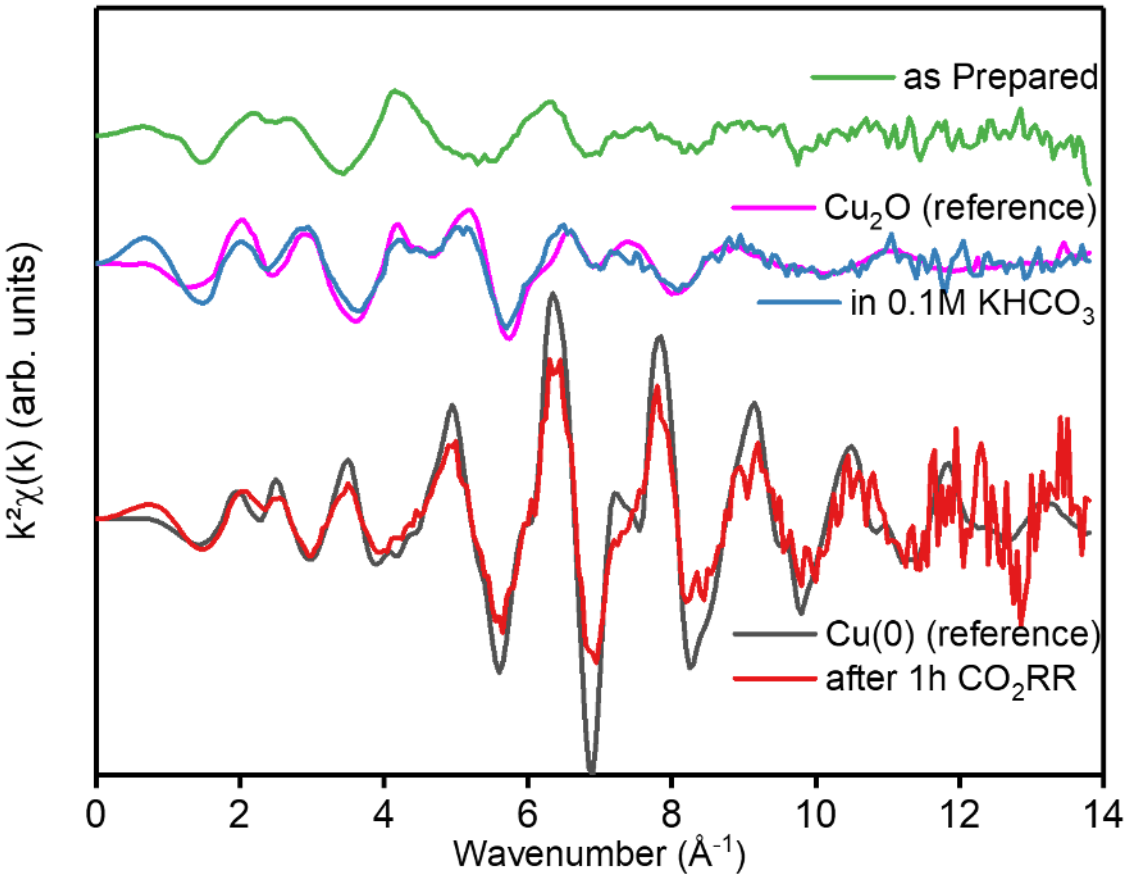

Figure S6: k-space EXAFS data of pristine Cu nanocubes acquired under *operando* conditions during CO_2 electroreduction at -1.1 V vs. RHE in 0.1 M $KHCO_3$. Data from the as prepared sample, a metallic Cu reference, and a Cu_2O reference sample, all measured in air, are also included for comparison.

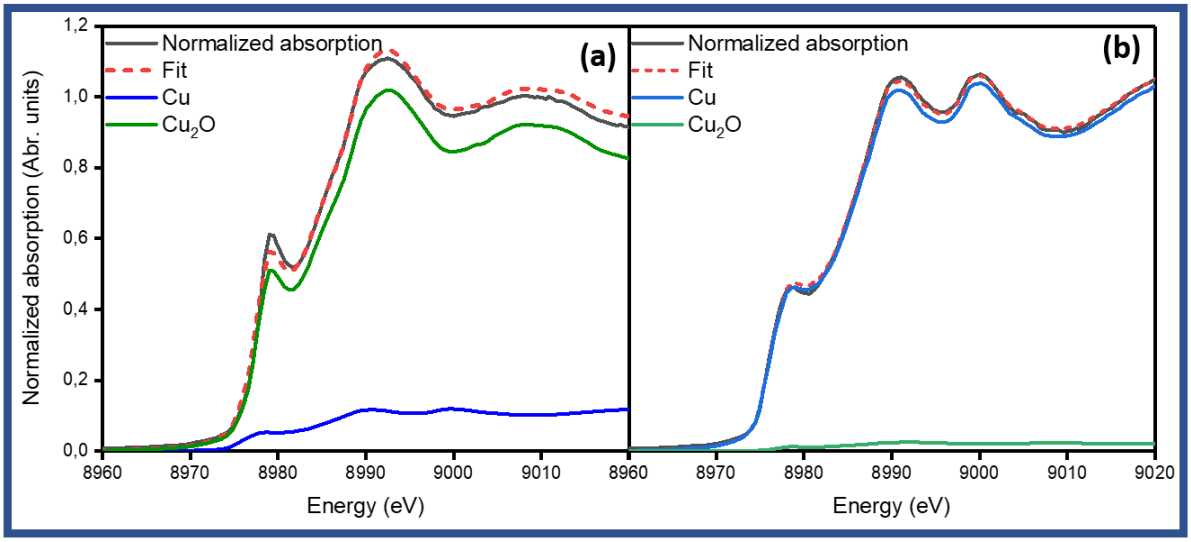

Figure S7: Deconvolution of the XANES region of Cu nanocube samples. On the left, a linear combination fit of the pristine Cu-cubes in 0.1 M $KHCO_3$ before and on the right after 1 h of CO_2RR at -1.1 V vs RHE is shown.

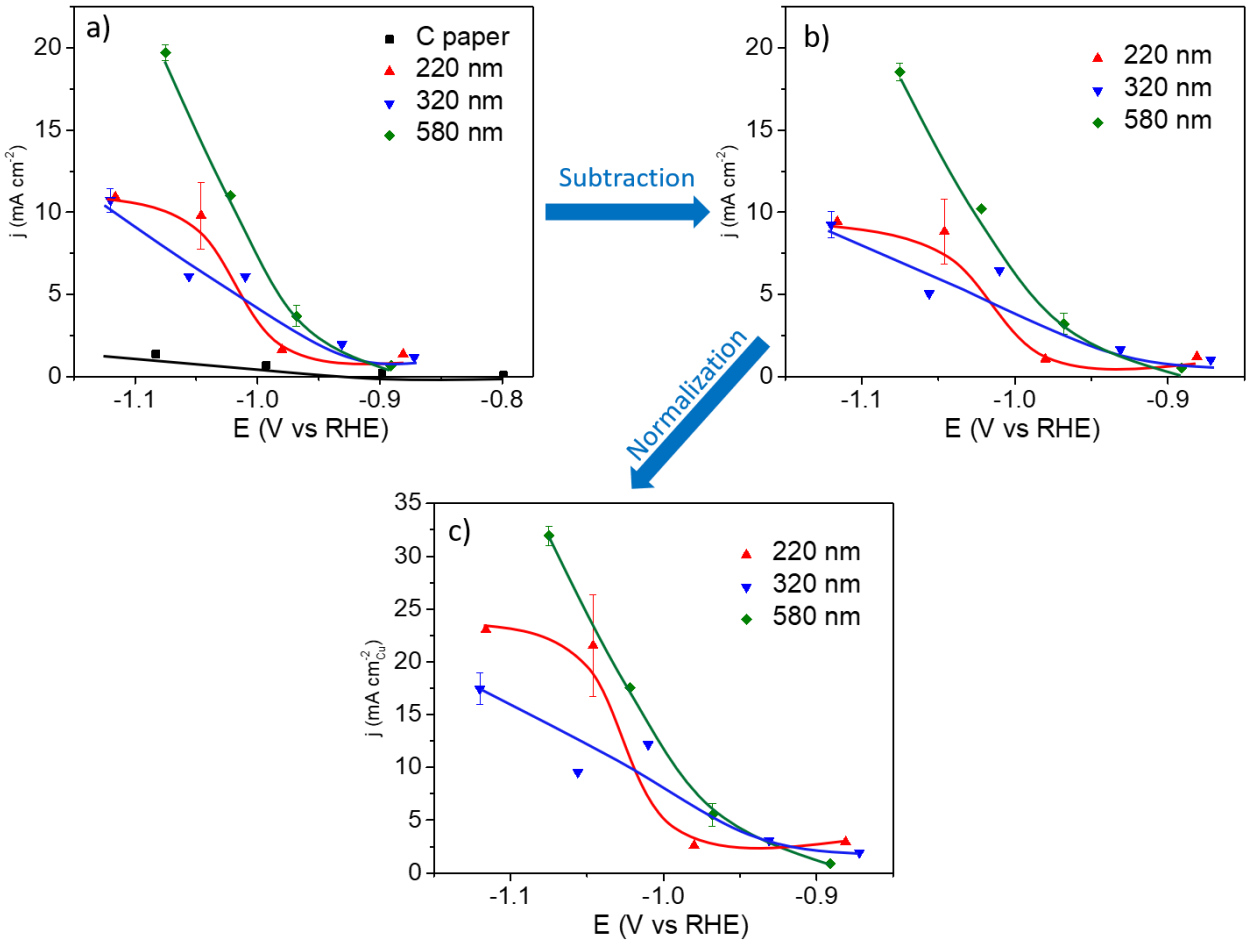

Figure S8: (a) Geometric current density of pristine Cu-cubes with an average size of 220, 320, and 580 nm and the clean C-paper support at potentials between -1.15 V and -0.85 V vs RHE. The contribution from the C-paper support was subtracted in (b). The data in (a) and (b) and shown normalized by the total sample area, which includes the cubes and the carbon support. In (c), the data are normalized by the real Cu surface area extracted from the analysis of SEM images.

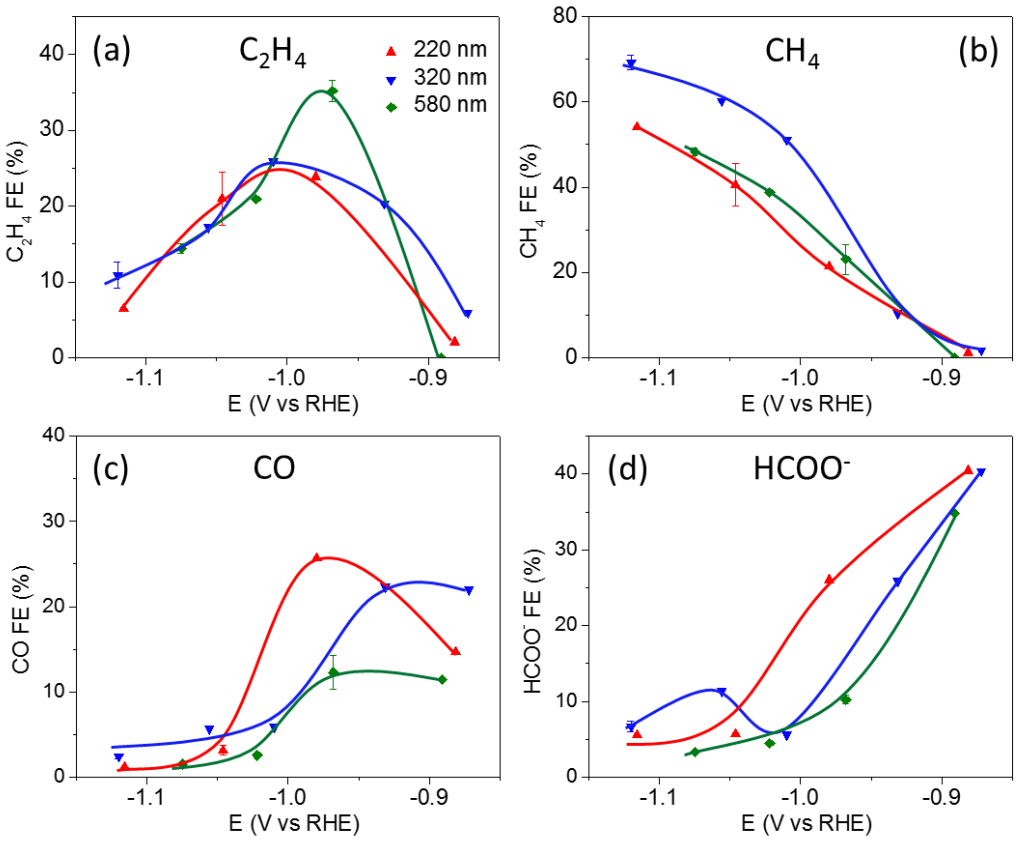

Figure S9: Faradaic efficiency for ethylene (a), methane (b), carbon-monoxide (c), and formate (d) obtained after 1 hour of CO_2RR at different potentials. The products produced by a reference blank substrate scaled to the (approximate) unoccupied carbon paper in the samples was subtracted to show only the products from the Cu-cubes.

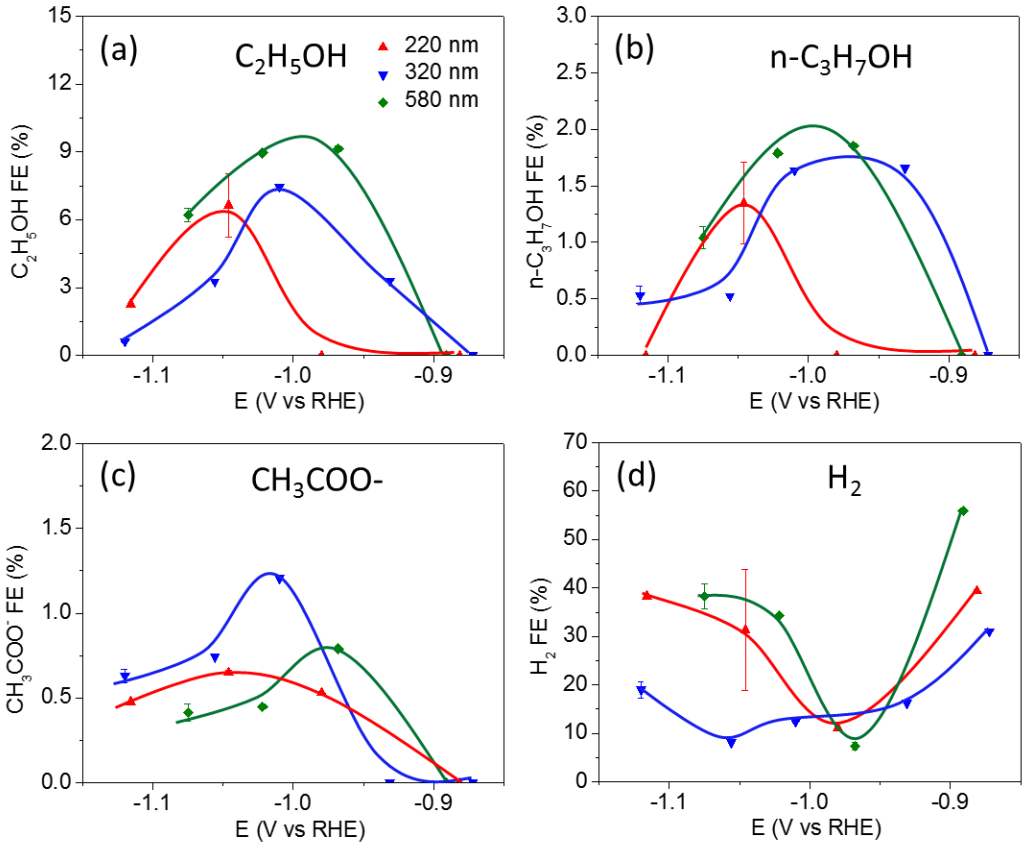

Figure S10: Faradaic efficiency for ethanol (a), 1-propanol (b), acetate (c), and hydrogen (d) after 1 hour of CO_2RR at different potentials.

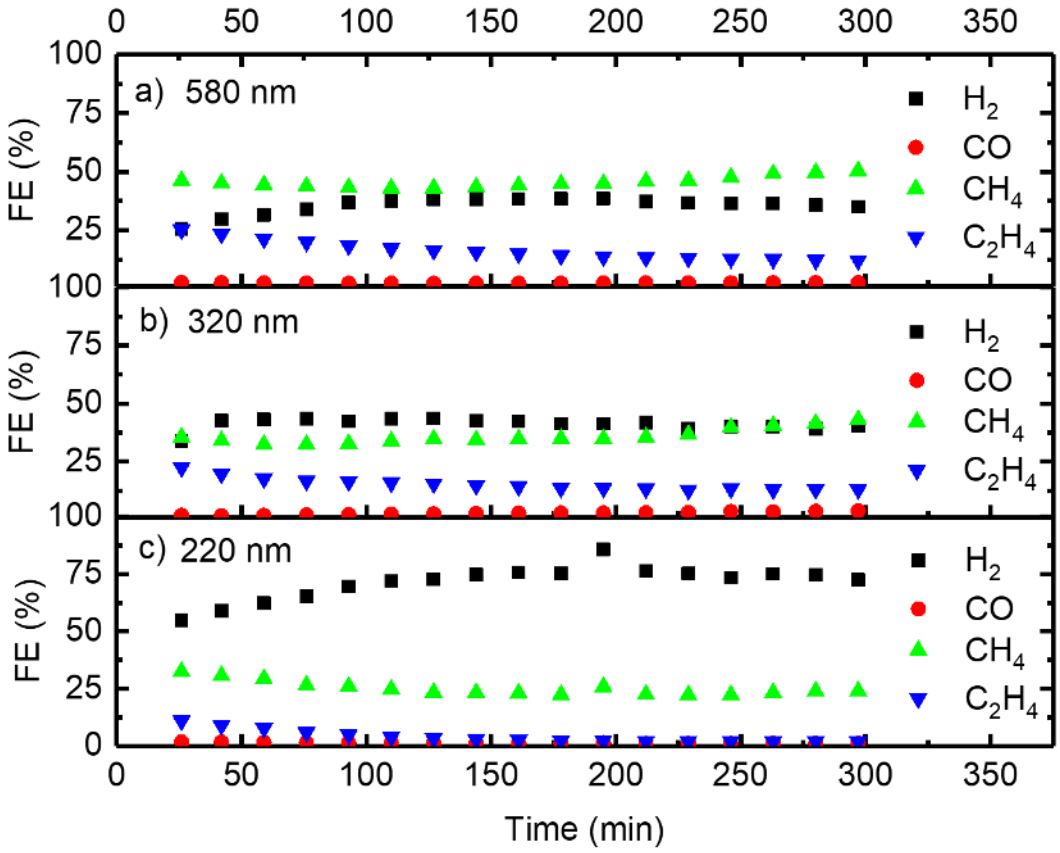

Figure S11: Temporal evolution of the product selectivity during CO_2RR for 580 nm (a), 320 nm (b), and 220 nm (c) Cu nanocubes measured at -1.05 V vs RHE for 5 hours. For smaller cube sizes, H_2 production outweighs the production of hydrocarbons, whilst on the bigger and more morphologically stable Cu-nanocubes this trend reverses.

[1] D. Gao, I. Zegkinoglou, N. J. Divins, F. Scholten, I. Sinev, P. Grosse, B. Roldan Cuenya, *ACS Nano* **2017**, *11*, 4825–4831.

[2] J. Timoshenko, A. Kuzmin, *Comput. Phys. Commun.* **2009**, *180*, 920–925.

[3] Y. Hori, R. Takahashi, Y. Yoshinami, A. Murata, *J. Phys. Chem. B* **1997**, *101*, 7075–7081.

[4] K. J. P. Schouten, E. Pérez Gallent, M. T. M. Koper, *J. Electroanal. Chem.* **2014**, *716*, 53–57.

[5] A. S. Varela, W. Ju, T. Reier, P. Strasser, *ACS Catal.* **2016**, *6*, 2136–2144.

[6] M. C. Biesinger, L. W. M. Lau, A. R. Gerson, R. S. C. Smart, *Appl. Surf. Sci.* **2010**, *257*, 887–898.